

Fabrication of an Rb–Xe gas cell with optical components attached by optical contact bonding for an atom spin gyroscope

SANG HYUK HONG, SIN HYUK YIM,* TAEK JEONG, JEONG BIN NAM, AND SANGKYUNG LEE

Agency for Defense Development, Daejeon 34186, Republic of Korea

*seamouse@add.re.kr

Received 2 January 2025; revised 15 April 2025; accepted 16 April 2025; posted 18 April 2025; published 6 May 2025

We describe the fabrication of a cubic Rb–Xe gas cell integrated with optical components. Two prism mirrors and a reflection mirror are attached to the Rb–Xe gas cell by optical contact bonding. This concept was studied by using free induction decay measurements of Xe gas with two diode lasers at 795 nm in a magnetic shield. The transverse spin relaxation times of ^{129}Xe and ^{131}Xe are 7.0 s and 7.2 s, respectively, with sufficient signal amplitude. Optical contact bonding is shown to be promising to provide the monolithic atomic gas cell with optical components and the compact design of an atom spin gyroscope. © 2025 Optica Publishing Group. All rights, including for text and data mining (TDM), Artificial Intelligence (AI) training, and similar technologies, are reserved.

<https://doi.org/10.1364/AO.554573>

1. INTRODUCTION

Optical contact bonding is a powerful technique that can be used to combine two optical components into a monolithic unit without using any glue [1,2]. When two super-polished surfaces come into contact with each other, optical contact bonding is completed by the intermolecular forces between the two surfaces. Given that optical contact bonding is conducted at room temperature, does not have outgassing on the bonding surface, and is transparent, this method has been used to manufacture optical components such as prisms and polarizing beam splitters. For a high-quality factor cavity used in a ring laser gyroscope (RLG), mirrors are attached to a Zerodur block via optical contact bonding [3]. Super-polished wedged nano-cells have been fabricated and characterized to investigate atom–surface interactions [4]. In Ref. [4], a thick-wedged plate undergoes an optical contact process on one side of the inner surface of a cell to produce a thin wedge with a thickness ranging between 0 and 900 nm.

Atomic gas cells are essential parts of atomic sensors [5–7]. The type of alkali atoms and buffer gas varies depending on the intended use of the atomic sensor. When anodically bonded atomic gas cells are employed in chip-scale atomic clocks [8,9] and atomic magnetometers [10,11], glass-blown cells are used in saturated absorption spectroscopy [12,13], a Rydberg atom-based radio frequency receiver [14,15], and an atom spin gyroscope [16–18]. Princeton University developed a micro-fabricated atomic gas cell with ^3He , ^{129}Xe , and ^{87}Rb for comagnetometer application [19]. Xi'an Jiaotong University employed an inner-sidewall molding process to provide

multi-optical channels of an atomic gas cell with good optical clarity [20].

The atom spin gyroscope (ASG), also known as the nuclear magnetic resonance gyroscope (NMRG), measures rotation rates by counting the Larmor frequency of the nuclear spins of noble gases within an atomic gas cell. When a bias magnetic field is applied to the z axis as the quantization axis, a circularly polarized pump beam passes through the atomic gas cell along the z axis to pump the electron spins of the alkali atoms optically. During collisions between alkali atoms and noble gas nuclei, angular momentum is transferred to the nuclear spins of noble gases via hyperfine interactions. Subsequently, when an AC magnetic field resonant with the NMR frequency is applied in a transverse direction, the noble gas nuclear spins coherently precess about the bias magnetic field. Accordingly, the alkali atom spins undergo precession around the total magnetic field, which comprises the bias magnetic field and the nuclear magnetic moment of noble gases. When a linearly polarized probe beam is directed along the x axis, the atom–light interaction with the alkali atoms induces optical Faraday rotation in the probe beam's polarization. By analyzing the polarization of the probe beam, one can directly obtain information on the precession of noble gas nuclear spins. Furthermore, techniques such as lock-in-detection and dual-species operation then facilitate the extraction of the rotation rate from the shifts in the measured NMR frequency. The high sensitivity of *in situ* alkali-magnetometry is primarily attributed to the substantial enhancement provided by the Fermi-contact interaction during spin-exchange collisions, which establishes a strong hyperfine coupling between the electron spins of alkali atoms and the

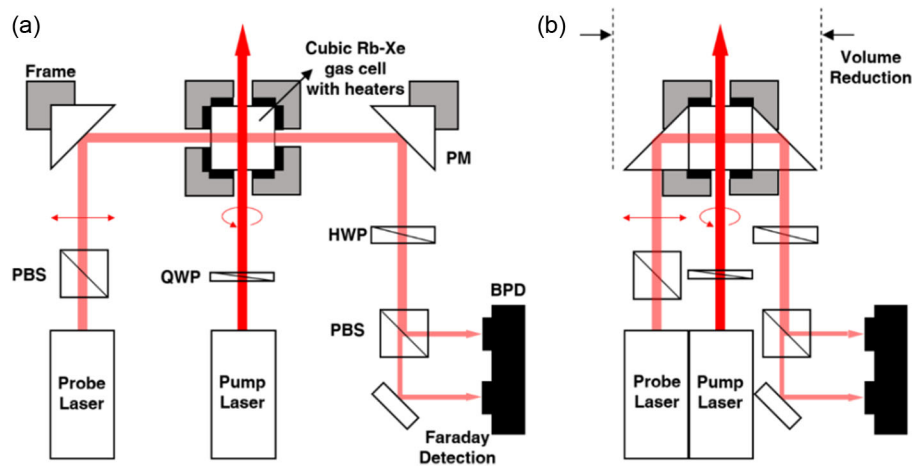


Fig. 1. (a) Schematic of the ASG, (b) schematic of the ASG based on an Rb–Xe gas cell with two prism mirrors attached by optical contact bonding. The frames holding the prism mirrors are removed, thereby reducing the volume of the ASG.

nuclear spins of noble gases, thereby amplifying the effective field in proportion to the nuclear magnetization [21]. Because the direction axis of the probe beam and pump beam are perpendicular to each other, cubic atomic gas cells filled with rubidium, xenon, nitrogen, and hydrogen gas are used [22]. Northrop Grumman developed a nuclear magnetic resonance gyroscope (NMRG) with a small volume (10 cc) in 2014 [23,24]. In that work, the direction of the probe beam is changed by a prism mirror, with the beam then passing through a glass-blown atomic gas cell. The frames to hold each part take up space in the setup, as shown in Fig. 1(a). The internal size of the cell is 2 mm. They employed VCSELs and compact optical components with MEMS fabrication to reduce the volume of the NMRG [23]. With regard to the performance of the NMRG, they showed an angular random walk of $0.005 \text{ deg/h}^{1/2}$ and bias stability of 0.01 deg/h .

In order to achieve a compact design while maintaining the performance of the ASG, it is important to integrate the optical components with an atomic gas cell. The sum of the lengths of the atomic gas cell, the prism mirrors, and the frames determines the diameter of the ASG. To remove the frames mounting the optical components shown in Fig. 1(a), one method is to attach the optical components and the atomic gas cells using glue [25,26]. The use of glue, however, can easily contaminate the optical components and make it difficult to achieve similar optical alignment between assemblies manufactured using the same process. Instead, we consider the possibility of using optical contact bonding in the ASG to provide the monolithic unit of the optics part containing an Rb–Xe gas cell, as shown in Fig. 1(b).

This article reports the fabrication of an Rb–Xe gas cell with two prism mirrors and a reflection mirror attached by optical contact bonding. The size of the cubic cell is 7.5 mm. Initially, the cell is filled with ^{87}Rb , ^{129}Xe , ^{131}Xe , N_2 , and H_2 for the ASG application [7]. The stem is sealed off using a torch. Then, the three surfaces of the Rb–Xe gas cell are polished to bond two prism mirrors and a reflection mirror. The free induction decay of the Xe gas is measured and investigated in a four-layer

magnetic shield on an optical table. The transverse spin relaxation times of ^{129}Xe and ^{131}Xe are 7.0 and 7.2 s, respectively. The optical contact bonding of the Rb–Xe gas cell with optical components guarantees a monolithic design, mechanical stability, and low outgassing [4,26,27]. Therefore, the techniques presented here can be used in various ways in atomic physics.

2. FABRICATION OF THE Rb–Xe GAS CELL

The fabrication process of the Rb–Xe gas cell is reported in Ref. [22]. A brief description is presented here. A cubic glass cell with a stem (made in China), composed of Pyrex, is prepared [28]. The outer length of the cubic cell is 7.5 mm, and the wall thickness is 1 mm. The outer and inner diameters of the stem are 2.5 and 1 mm, respectively. The inner surface of the cubic glass cell is washed 10 times each with distilled water, ethanol, and methanol. The cubic glass cell is baked at 550°C for two days in the air and three days under a vacuum. The cubic glass cell is then connected to a metallic chamber via a Wilson sealing adapter [29,30]. The metallic chamber is baked at 120°C while the cubic glass cell is baked at 450°C . The metallic chamber and the cubic glass cell are filled with nitrogen, which is purged by a turbopump. This process is repeated three times. The vacuum pressure at the turbopump reaches 1.0×10^{-9} Torr after a week. A copper container containing an ^{87}Rb ampule (BuyIsotope, isotopic enrichment 98.6 %) is heated to 90°C while the cubic glass cell is cooled at 5°C . Then, ^{87}Rb atoms are distilled into a cubic glass cell for three days until a sufficient amount of ^{87}Rb is gathered. Four gases (^{129}Xe , ^{131}Xe , N_2 , and H_2) are injected into the cubic glass cell via mass flow controllers. The stem is sealed by means of pinch-off glass welding using a small torch with oxygen. With pinch-off glass welding, sealing the stem takes 5 s.

When fabricating the Rb–Xe gas cell, two Pyrex prisms and a Pyrex circular window are initially prepared at Optonics (Gwangju, Korea). The fabrication process consists of two main stages: lapping and polishing. During the lapping process, the optics are mounted on the polishing pitch with fixtures. As the pitch rotates with the aluminum oxide abrasive, three surfaces of the prisms and two surfaces of the circular window undergo

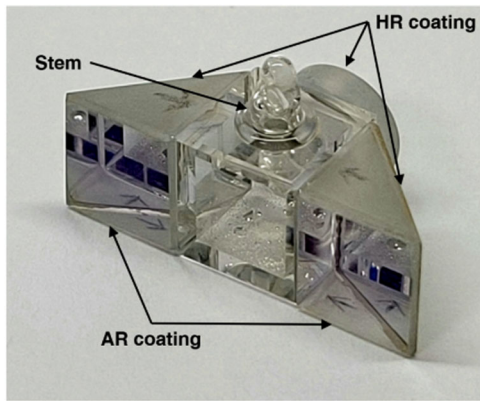


Fig. 2. Proposed Rb–Xe gas cell with two prism mirrors and a reflection mirror attached using optical contact bonding. The prism mirror changes the direction of a probe beam. A pump beam passes through the front side of the Rb–Xe gas cell and is then back-reflected by the reflection mirror. AR, anti-reflection; HR, high-reflection.

lapping. This stage typically takes less than two days, depending on the condition of the optics surface.

In the subsequent polishing process, the abrasive is replaced by cerium oxide. Polishing is performed in a clean room, and afterward, the surfaces are cleaned using cotton swabs and acetone to remove any contaminants within a week. The polished surfaces achieve a surface roughness below 0.1 nm. After polishing each surface, a high-reflection coating is applied to the oblique surface of the prism and the back side of the circular window.

Next, the Rb–Xe gas cell is transferred to Optonics and follows the identical process for the Rb–Xe gas cell, as above. The left, right, and back sides serve as the bonding surfaces. The optical contact bonding is carried out at room temperature and is completed within a day, ensuring a reliable process. The reflection mirror is attached to the back side, and two prism mirrors are attached to the left and right sides of the Rb–Xe gas cell, as shown in Fig. 2. The dimensions of the Rb–Xe gas cell with optical components are 22.5 mm × 10 mm × 12 mm, including the height of the stem. The total volume can be further reduced by fabricating a smaller cubic Rb–Xe gas cell with an outer dimension of 6 mm. Additional optical components, such as a half-wave plate and a quarter-wave plate, can also be attached to an Rb–Xe gas cell using optical contact bonding.

Although the fabricated Rb–Xe gas cell was attached to optical components by means of optical contact bonding, it is also possible to fabricate the Rb–Xe gas cell after bonding optical components to an empty cubic glass container. In this case, a high-temperature optical contact bonding method, known as deep optical contact bonding, can be employed. This allows the bonded monolithic assembly to undergo heat treatment up to 450°C. Additionally, the reflection mirror can be replaced with the high-reflection coating on the back side of the empty cubic glass container.

3. FREE INDUCTION DECAY OF Xe

Figure 3 describes the free induction decay (FID) measurements on an optical table to evaluate the transverse spin relaxation time (T_2) and signal amplitude of Xe gas.

The optical contact-bonded Rb–Xe gas cell is placed inside a four-layer magnetic shield (MS-1, Twinleaf). Two DBR lasers are employed, one as a pump beam and the other as a probe beam. The pump beam (PH795DBR, Photodigm), with a power of 27 mW and a diameter of 5 mm, operates at a wavelength of 795 nm, with a resonant D1 transition of ^{87}Rb . The pump beam is directed toward the Rb–Xe gas cell via an aperture located at the front center position of the magnetic shield. The reflection mirror attached to the Rb–Xe gas cell reflects the pump beam, thereby facilitating effective optical pumping. The electron spins of ^{87}Rb atoms are polarized on the z axis. The probe beam (PH795DBR, Photodigm), with a power of 3 mW and a diameter of 4 mm, is incident through a left-hand hole at the front of the magnetic shield. The prism mirror changes the direction of the probe beam perpendicular to the pump beam in the region of the Rb–Xe gas cell. The Faraday rotation is measured at a balanced photodetector (PDB210A/M, Thorlabs). The Rb–Xe gas cell is heated to 80°C to ensure efficient spin-exchange collisions between ^{87}Rb and $^{129}\text{Xe}/^{131}\text{Xe}$. Two double-layer polyimide film heaters are installed on the two sides of the Rb–Xe gas cell that are along the path of the pump beam [31]. A temperature sensor (PT 1000) is placed at the bottom of the Rb–Xe gas cell.

Following several minutes of optical pumping, the nuclear spins of Xe, initially oriented along the z axis via spin-exchange collisions with polarized ^{87}Rb , are tipped off onto the xy plane by an oscillating magnetic field generated by the x coil. This field has the form of $B_x \sin(\omega_0 t)$, satisfying the $\pi/2$ -pulse condition: $\gamma B_x \tau_{\pi/2}/2 = \pi/2$ with a pulse duration of $\tau_{\pi/2}$. Here, $\omega_0 = \gamma B_0$ represents the Larmor frequency of nuclear spins of Xe, where γ denotes the gyromagnetic ratio of Xe, and B_0 indicates the magnitude of the bias magnetic field. The gyromagnetic ratios of ^{129}Xe and ^{131}Xe are $2\pi \times 11.777$ MHz/T and $2\pi \times 3.516$ MHz/T, respectively. Given a B_0 of 2.80 μT in this experiment, the measured Larmor frequencies were 33.0 Hz for ^{129}Xe and 9.84 Hz for ^{131}Xe . In this experiment, oscillating magnetic fields of $B_x = 0.34$ μT were applied for 0.12 and 0.42 s, respectively, satisfying the $\pi/2$ -pulse condition for ^{129}Xe and ^{131}Xe . Immediately after the $\pi/2$ -pulse, the total magnetization produced by the nuclear spins of Xe undergoes precession around the bias magnetic field, with the z -component recovering over time. The linearly polarized probe beam, which is off-resonant with the D1 transition of ^{87}Rb , exhibits rotation of the polarization plane proportional to the x component of the Xe magnetization, resulting in optical Faraday rotation, as shown in Fig. 4.

The FID signal is determined by the sum of two distinct signals: the single exponential-decay-sinusoidal signal of ^{129}Xe and the triple exponential-decay-sinusoidal signal from the triplet structure of ^{131}Xe , which is a consequence of the quadrupole interactions. After filtering for the respective Larmor frequencies, the T_2 values of ^{129}Xe and ^{131}Xe can be estimated. The T_2 value is determined to be 7.0 s for ^{129}Xe by fitting the upper envelope based on $A \exp(-t/T_2) + B$ in Fig. 4(a). In contrast, for cases of diamagnetic atoms where $I \geq 1$, such as ^{131}Xe , the quadrupole interactions with the electric field gradients must be considered due to the asymmetric geometries and surface properties of the cell [32]. These quadrupole interactions manifest as an oscillating upper envelope in the FID signal.

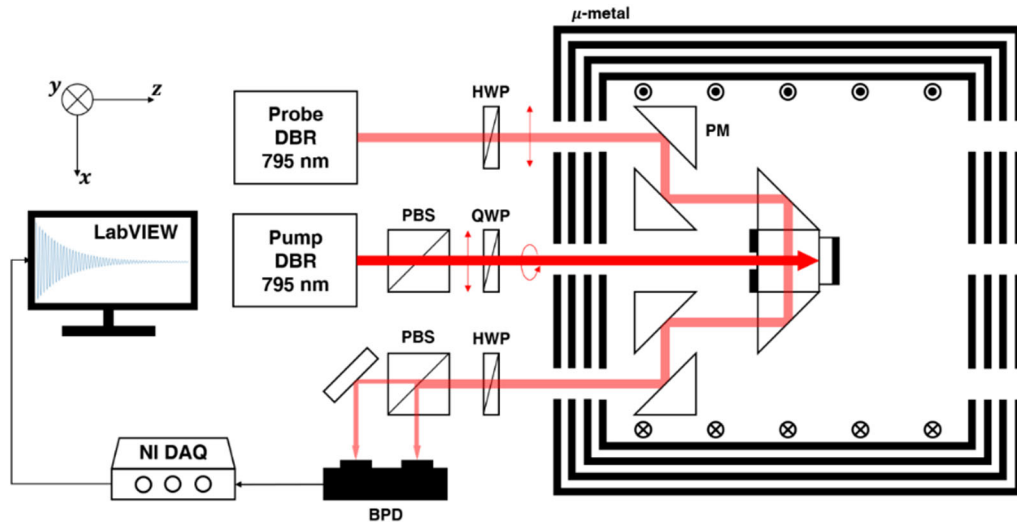


Fig. 3. Schematic for the FID measurements. A pump beam is introduced in the Rb–Xe gas cell and reflected back, orienting the electron spins of ^{87}Rb along the z axis. A bias magnetic field on the z axis and AC pulses on the x axis are generated by a coil wound on the inner surface of the innermost μ -metal. A probe beam is directed toward the x axis to measure the polarization of the electron spins of ^{87}Rb . DBR, distributed Bragg reflector; HWP, half-wave plate; QWP, quarter-wave plate; PBS, polarizing beam splitter; PM, prism mirror; BPD, balanced photodetector.

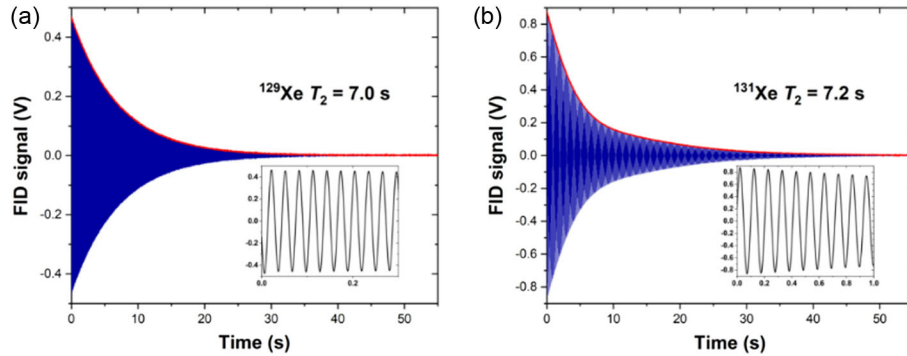


Fig. 4. FID results for ^{129}Xe and ^{131}Xe , where the temperature of the Rb–Xe gas cell is 80°C . The red solid line represents the upper envelope of the FID signal. The corresponding insets depict the FID signals of ^{129}Xe and ^{131}Xe between 0 and 1 s. (a) The T_2 value of ^{129}Xe is 7.0 s, while the Larmor frequency of ^{129}Xe is 33.0 Hz. (b) The T_2 value of ^{131}Xe is 7.2 s, while the Larmor frequency of ^{131}Xe is 9.84 Hz.

The T_2 value of ^{131}Xe is determined to be 7.2 s by fitting the upper envelope of the measured FID signal to the function $A_Q(1 + B_Q\cos(\omega_Q t + \varphi_Q))\exp(-\frac{t}{T_2}) + C_Q$, where ω_Q is 0.16 Hz, represents the beating frequency induced from the quadrupole interaction, as shown in Fig. 4(b).

The longitudinal spin relaxation time (T_1) is also measured through the inversion-recovery method because T_1 provides the upper limit of the transverse spin relaxation time. The inversion-recovery method involves varying the delay time between π and $\pi/2$ pulses while recording the initial amplitude of the FID signal for each delay time [33]. Figure 5 provides the extracted T_1 results after fitting the plot to $|A(1 - B\exp(-t/T_1))|$ for both ^{129}Xe and ^{131}Xe . The T_1 values of ^{129}Xe and ^{131}Xe are 12.9 and 12.1 s, respectively. In contrast to the longitudinal relaxation due to spin-lattice interactions, the transverse relaxation additionally includes dephasing due to spin-spin interactions. As nuclear spins diffuse through a spatially inhomogeneous magnetic field, they experience local field fluctuations. These fluctuations induce dephasing among

the spins, thereby disrupting phase coherence and thereby promoting transverse relaxation [34,35].

The transverse spin relaxation times and the amplitudes of the FID signal of Xe in this experiment are comparable to earlier results by the authors [36,37]. Thus, we expect that the Rb–Xe gas cell with optical components attached by optical contact bonding will reduce the volume of an ASG without degrading its performance.

When four optical windows of an atomic vapor cell are used in atomic physics experiments [36–39], in general, four heaters are employed to prevent alkali atoms from accumulating on the optical windows. The windows coated with alkali atoms attenuate the power of the laser and decrease the signal-to-noise ratio (SNR) of the experiments. Because two prism mirrors are attached to either side of the cubic Rb–Xe gas cell in our experiment, only two heaters are utilized: a square-shaped heater with a central aperture positioned at the front of the Rb–Xe gas cell and a circular heater placed at the back of the reflection mirror, as shown in Fig. 3. It is, therefore, crucial to assess whether the

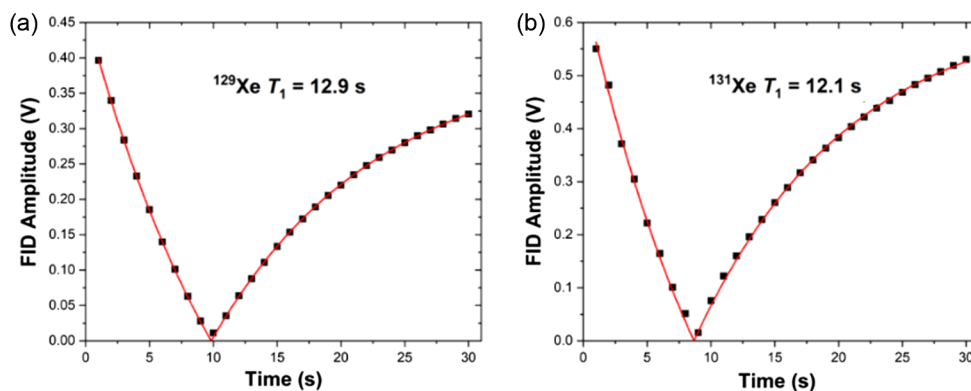


Fig. 5. (a), (b) Inversion-recovery method results for ^{129}Xe and ^{131}Xe at 80°C , respectively. The x axis of each plot represents the time interval between successive π and $\pi/2$ -pulses, while the y axis depicts the amplitude of the FID signal at each time interval. From the fitting results, the T_1 values of ^{129}Xe and ^{131}Xe are 12.9 and 12.1 s, respectively.

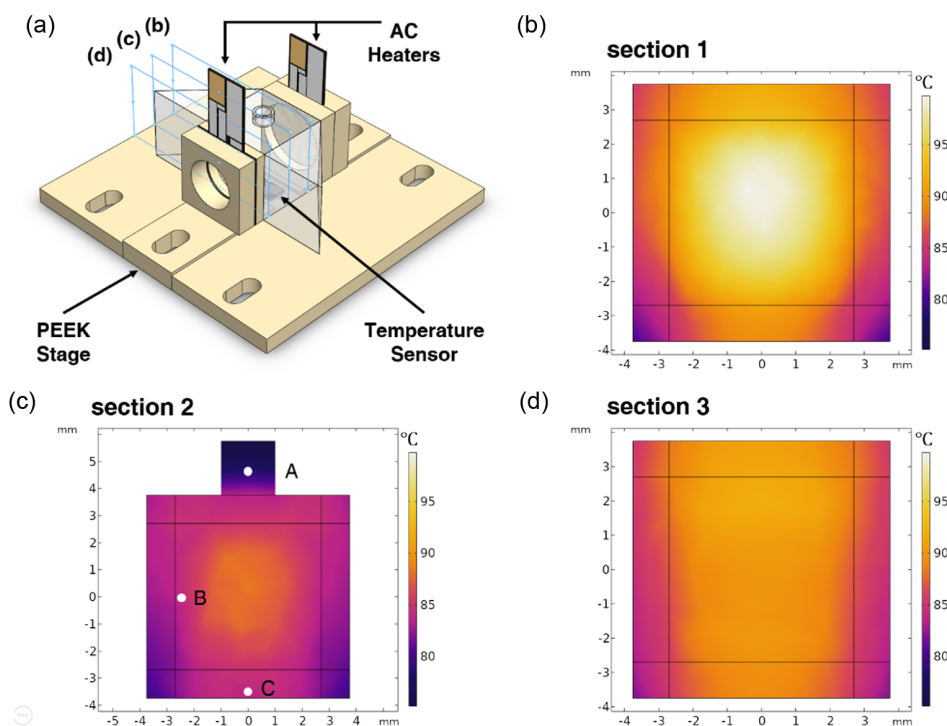


Fig. 6. (a) Illustration of the Rb–Xe gas cell with two heaters for a thermal simulation. The three slice plots represent the following; (b) Section 1, the inner surface of the Rb–Xe gas cell where the reflection mirror is attached; (c) Section 2, the central cross section including the stem; (d) Section 3, the inner surface of the front side of the cell. The heating power is adjusted so that the temperature at point C, located on the outer bottom surface of the cell where the temperature sensor was in contact, reached 83°C at thermal equilibrium. Meanwhile, the surfaces in contact with the heaters ((b) and (d)) exhibit the highest temperatures at the central regions, reaching 99°C and 91°C , whereas the inner corners and sides show the lowest temperatures, at 85°C and 86°C , respectively. However, the temperature at point A, located in the stem, is approximately 78°C , which is 5°C lower than point B, located on the inner surface of the cell side where the prism mirror is attached. Meanwhile, the temperature near the center of (c) is approximately 88°C , indicating a non-uniform temperature distribution of a quadratic nature between two heaters.

use of only two heaters contributes to the accumulation of alkali atoms on the optical windows.

We conduct thermal simulations based on a finite element analysis using COMSOL software to study the temperature distribution of the Rb–Xe gas cell with optical components attached. The heat exchange is primarily modeled as a combination of natural convection with the surrounding ambient air, maintained at room temperature, and thermal conduction at the contact interfaces with the surfaces of the stage and a

temperature sensor in contact with the cell. The power applied to the two heaters used in this case is adjusted to set the temperature sensor to 83°C . To facilitate the analysis, the regions of the Rb–Xe gas cell are divided into three distinct sections: (Section 1) the inner surface of the cell where the reflection mirror is attached, (Section 2) the central cross-section across the stem, and (Section 3) the inner surface at the front side of the cell.

Figures 6(b)–6(d) show the temperature distribution for Sections 1–3. In Section 1, the center shows the highest temperature at 99°C, while the temperature of the lower inner corner of the Rb–Xe gas cell is 85°C. In Section 3, the center again shows the highest temperature at 91°C, with the inner side at 86°C. In contrast, the stem shows the lowest temperature at 78°C, while the temperatures at the inner side and corner are 83°C, as indicated in Section 2. This difference is due to the distance from the heaters and the protruding geometry of the stem, which increases the surface area for heat exchange with the surrounding air. Note that the temperature on the inner side is higher than the temperature at the stem; therefore, alkali atoms may accumulate around the stem. Empirical observations after more than one month of heating of the Rb–Xe gas cell, as described in Fig. 6, reveal that Rb vapor condenses near the stem.

The temperature distribution between the two heaters, however, exhibits quadratic variation, as shown in Figs. 6(b)–6(d). The presence of temperature gradients induces thermal diffusion, leading to relative concentration gradients between ^{129}Xe and ^{131}Xe , which in turn cause observable shifts in their effective resonance frequencies [40,41]. Because the deviation in the rotation rate is simply expressed as $\sigma(\Omega) = \sqrt{(\frac{\gamma_{129}}{\gamma_{131}-\gamma_{129}})^2 \sigma^2(\omega_{131}) + (\frac{\gamma_{131}}{\gamma_{131}-\gamma_{129}})^2 \sigma^2(\omega_{129})}$, such shifts could lead to the drifts in bias stability of the ASG [37]. Consequently, the subsequent study will investigate effective remedial strategies aimed at mitigating these temperature gradients. Potential solutions include installing supplementary heaters on the prism mirrors or arranging heaters symmetrically by employing a direct high-reflection coating on the cell surface as a substitute for the reflection mirror.

4. CONCLUSION

We present a cubic Rb–Xe gas cell with optical components attached by optical contact bonding that could be used as an optical part of an atom spin gyroscope. Transverse spin relaxation times and amplitudes of free induction decay measurement of Xe gas in the Rb–Xe gas cell are found to be comparable to those in Refs. [36,37]. The provision of the monolithic unit of the optical part by means of optical contact bonding facilitates easy optical alignment and a compact design of the atom spin gyroscope. In the context of vacuum packaging for the atom spin gyroscope, optical contact bonding without using adhesive is useful in eliminating outgassing.

Funding. Agency for Defense Development.

Disclosures. The authors declare no conflicts of interest.

Data availability. Data underlying the results presented in this paper are not publicly available at this time but may be obtained from the authors upon reasonable request.

REFERENCES

- S. R. John, "A study of glass surfaces in optical contact," *Proc. R. Soc. Lond. A* **156**, 326–349 (1936).
- G. Kalkowski, S. Risse, C. Rothhardt, *et al.*, "Optical contacting of low-expansion materials," *Proc. SPIE* **8126**, 81261F (2011).
- K. U. Schreiber and J.-P. R. Wells, "Invited review article: large ring lasers for rotation sensing," *Rev. Sci. Instrum.* **84**, 041101 (2013).
- T. Peyrot, C. Beurthe, S. Coumar, *et al.*, "Fabrication and characterization of super-polished wedged borosilicate nano-cells," *Opt. Lett.* **44**, 1940–1943 (2019).
- S. Knappe, V. Shah, P. D. D. Schwindt, *et al.*, "A microfabricated atomic clock," *Appl. Phys. Lett.* **85**, 1460–1462 (2004).
- I. K. Kominis, T. W. Kornack, J. C. Allred, *et al.*, "A subfemtotesla multichannel atomic magnetometer," *Nature* **422**, 596–599 (2003).
- T. W. Kornack, R. K. Ghosh, and M. V. Romalis, "Nuclear spin gyroscope based on an atomic comagnetometer," *Phys. Rev. Lett.* **95**, 230801 (2005).
- S. Knappe, V. Gerginov, P. D. D. Schwindt, *et al.*, "Atomic vapor cells for chip-scale atomic clocks with improved long-term frequency stability," *Opt. Lett.* **30**, 2351–2353 (2005).
- G. D. Martinez, C. Li, A. Staron, *et al.*, "A chip-scale atomic beam clock," *Nat. Commun.* **14**, 3501 (2023).
- P. D. D. Schwindt, S. Knappe, V. Shah, *et al.*, "Chip-scale atomic magnetometer," *Appl. Phys. Lett.* **85**, 6409–6411 (2004).
- V. Gerginov, M. Pomponio, and S. Knappe, "Scalar magnetometry below 100 fT/Hz^{1/2} in a microfabricated cell," *IEEE Sens. J.* **20**, 12684–12690 (2020).
- P. Chang, D. Pan, H. Shang, *et al.*, "A global crossover saturated-absorption spectroscopy induced by dual-frequency laser," *J. Phys. B: At. Mol. Opt. Phys.* **53**, 205402 (2020).
- R. Bala, J. Ghosh, and V. Venkataraman, "Impact of Zeeman sub-level pumping on saturated absorption spectra of thermal atomic vapor," *Appl. Phys. B* **130**, 13 (2024).
- S. M. Bohaichuk, D. Booth, K. Nickerson, *et al.*, "Origins of Rydberg-atom electrometer transient response and its impact on radio-frequency pulse sensing," *Phys. Rev. Appl.* **18**, 034030 (2022).
- Z. Song, H. Liu, X. Liu, *et al.*, "Rydberg-atom-based digital communication using a continuously tunable radio-frequency carrier," *Opt. Express* **27**, 8848–8857 (2019).
- D. Meyer and M. Larsen, "Nuclear magnetic resonance gyro for inertial navigation," *Gyroscopy Navig.* **5**, 75–82 (2014).
- H. Yu, M. W. Park, S. W. Choi, *et al.*, "Measuring scale factor of atomic spin gyroscope and closed-loop operation," *AIP Adv.* **10**, 075209 (2020).
- G. Gao, J. Hu, F. Tang, *et al.*, "Stability improvement of nuclear magnetic resonance gyroscope with self-calibrating parametric magnetometer," *Phys. Rev. Appl.* **21**, 014042 (2024).
- M. E. Limes, N. Dural, M. V. Romalis, *et al.*, "Long spin-1/2 noble gas coherence times in mm-sized anodically bonded batch-fabricated ^3He - ^{129}Xe - ^{87}Rb cells," *Appl. Phys. Lett.* **126**, 134001 (2025).
- M. Yu, Y. Chen, Y. Wang, *et al.*, "Microfabricated atomic vapor cells with multi-optical channels based on an innovative inner-sidewall molding process," *Engineering* **35**, 46–55 (2024).
- B. C. Grover, "Noble-gas NMR detection through noble-gas-rubidium hyperfine contact interaction," *Phys. Rev. Lett.* **40**, 391 (1978).
- S. H. Yim, D.-Y. Lee, S. Lee, *et al.*, "Experimental setup to fabricate Rb–Xe gas cells for atom spin gyroscopes," *AIP Adv.* **12**, 015025 (2022).
- M. Larsen and M. Bulatowicz, "Nuclear magnetic resonance gyroscope: for DARPA's micro-technology for positioning, navigation and timing program," in *Proc. IEEE Int. Symp. Inertial Sensors Syst. (ISISS)* (2014), pp. 1–5.
- T. G. Walker and M. S. Larsen, "Spin-exchange-pumped NMR Gyros," *Adv. At., Mol., Opt. Phys.* **65**, 373–401 (2016).
- S. A. Knappe, H. G. Robinson, and L. Hollberg, "Microfabricated saturated absorption laser spectrometer," *Opt. Express* **15**, 6293–6299 (2007).
- K. Sosa, J. Oreggioni, and H. Failache, "Miniaturized saturated absorption spectrometer," *Rev. Sci. Instrum.* **91**, 083101 (2020).
- S. Kobtsev, S. Donchenko, S. Khripunov, *et al.*, "CPT atomic clock with cold-technology-based vapour cell," *Opt. Laser Technol.* **119**, 105634 (2019).
- <https://www.made-in-china.com>.
- R. R. Wilson, "A vacuum-tight sliding seal," *Rev. Sci. Instrum.* **12**, 91 (1941).
- S. R. Breeze, S. Lang, I. Moudrakovski, *et al.*, "Coatings for optical pumping cells and short-term storage of hyperpolarized xenon," *J. Appl. Phys.* **87**, 8013–8017 (2000).

31. S. H. Yim, Z. Kim, S. Lee, *et al.*, "Note: double-layered polyimide film heater with low magnetic field generation," *Rev. Sci. Instrum.* **89**, 116102 (2018).
32. Y.-K. Feng, S.-B. Zhang, Z.-T. Lu, *et al.*, "Electric quadrupole shifts of the precession frequencies of ^{131}Xe atoms in rectangular cells," *Phys. Rev. A* **102**, 043109 (2020).
33. H. Y. Carr and E. M. Purcell, "Effects of diffusion on free precession in nuclear magnetic resonance experiments," *Phys. Rev.* **94**, 630 (1954).
34. G. D. Cates, S. R. Schaefer, and W. Happer, "Relaxation of spins due to field inhomogeneities in gaseous samples at low magnetic fields and low pressures," *Phys. Rev. A* **37**, 2877 (1988).
35. D.-Y. Lee, S. Lee, and S. H. Yim, "Measurement of a ^{129}Xe transverse relaxation rate without the influence of Rb polarization-induced magnetic gradient," *Appl. Opt.* **60**, 7290–7296 (2021).
36. S. Lee, S. H. Yim, T. H. Kim, *et al.*, "Lock-in-detection in ^{87}Rb - $^{129}\text{Xe}/^{131}\text{Xe}$ atom spin gyroscopes," *J. Phys. B* **53**, 035502 (2020).
37. S. Lee, D. Y. Lee, K. M. Shim, *et al.*, "Performance comparison between ^{87}Rb -natural Xe-N_2 and ^{87}Rb - ^{129}Xe - ^{131}Xe - N_2 atom spin gyroscopes," *J. Korean Phys. Soc.* **78**, 203–209 (2021).
38. X. Wang, J. Li, C. Qu, *et al.*, "Method to quickly estimate T_1 value by suppressing spin exchange relaxation and magnetic field gradient relaxation in atomic sensors," *Opt. Express* **32**, 15380–15389 (2023).
39. W. Tengyue, P. Jinpeng, L. Zhanchao, *et al.*, "Optical magnetic combination method for suppressing the Rb polarization-induced magnetic gradient in Rb-Xe NMR comagnetometers," *Opt. Express* **31**, 17663–17676 (2023).
40. D. Sheng, A. Kabcenell, and M. V. Romalis, "New classes of systematic effects in gas spin comagnetometers," *Phys. Rev. Lett.* **113**, 163002 (2014).
41. H. Tian, G. Liu, Z. Liu, *et al.*, "The frequency shift of ^{129}Xe and ^{131}Xe nuclei in NMR sensors caused by weak temperature gradients," *Measurement* **214**, 112723 (2023).